INTERNATIONAL JOURNAL FOR NUMERICAL METHODS IN FLUIDS, VOL. 11, 479–499 (1990)

GSMAC FINITE ELEMENT METHOD FOR UNSTEADY INCOMPRESSIBLE NAVIER–STOKES EQUATIONS AT HIGH REYNOLDS NUMBERS

T. TANAHASHI AND H. OKANAGA

Faculty of Science and Technology, Keio University, 3-14-1 Hiyoshi, Kohoku-ku, Yokohama, 223 Japan

AND

T. SAITO

Research Laboratory of Asahi Glass Co., Ltd., 1150 Matubara, Hazawa, Kanagawa-ku, Yokohama, 221 Japan

SUMMARY

A new finite element technique is developed for predicting the velocity and the pressure in transient incompressible viscous fluid flows at high Reynolds numbers. The new method is based on the generalized and simplified marker-and-cell method (GSMAC) and has two characteristics: one is an application of the Bernoulli function and the implicit pressure solution algorithm to the explicit fractional time step method; the other is a high-order flux calculation to prevent the pressure field from oscillating. Two examples, driven cavity flows at high Reynolds numbers and vortex shedding behind a circular cylinder, are presented. Satisfactory agreement with experiment is demonstrated.

KEY WORDS GSMAC finite element method Incompressible Navier–Stokes solver High Reynolds number Driven cavity flow Vortex shedding behind a circular cylinder

1. INTRODUCTION

Numerical solutions of the Navier–Stokes equations for two-dimensional flows of incompressible fluid are generally given in terms of velocity and pressure or streamfunction and vorticity. The former formulation may be preferable because the treatment of boundary conditions is not only direct and easy but also extensible to three dimensions. The major difficulties arising with the primitive variable formulation are connected with the enforcement of a suitable approximation of the incompressibility constraint and the computation of pressure.[1,2] The MAC (marker-and-cell) finite difference scheme[3] has overcome these difficulties using a staggered mesh as shown in Figure 1(a), but it has less generality because of the required orthogonality of co-ordinates. On the other hand, the finite element method in which the pressure, like the velocity, is defined at the nodes of each element can lead to spurious numerical oscillations in the pressure field.

In the present paper a new finite element method is proposed which is analogous to the SMAC[4] and the HSMAC[5] schemes and is called the GSMAC (generalized and simplified MAC) scheme.[1,6,7] The variables in the GSMAC scheme are velocity and total energy[8,9] instead of velocity and pressure. The MAC scheme is based on velocity components defined at the cell mid-sides and does not produce any oscillations in the field variables. The GSMAC extension of the

0271–2091/90/130479–21$10.50

Received 13 November 1988
Revised 2 August 1989

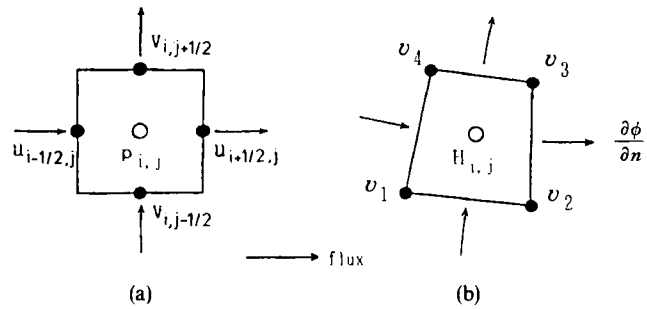

Figure 1. MAC scheme and GSMAC scheme in 2D: (a) MAC scheme; (b) GSMAC element

SMAC and HSMAC schemes is shown in Figure 1(b) for the two-dimensional case. The velocity staggering due to equation (7) is like the SMAC scheme and the pressure correction due to step 4 in Section 3.2 is like the HSMAC scheme.

When the same interpolation functions are employed for pressure and velocity, velocity oscillations are produced. However, these oscillations are eliminated by making the interpolation function for pressure one order less than the interpolation function for velocity.

When a fine mesh is used, low-order approximations are more economical in CPU time than high-order approximations. Hence the lowest interpolation functions are adopted in the GSMAC method: piecewise bilinear in 2D or trilinear in 3D for the velocity and constant over each element for the total energy. As benchmark problems, the flow in a driven cavity and vortex shedding behind a circular cylinder are examined at high Reynolds numbers.

2. PROBLEM FORMULATION

We consider here a flow in a cavity in the domain depicted in Figure 4(a) (see Section 4). The equations governing the flow are the equation of momentum written in rotational form and the equation of continuity written in solenoidal form:

$$\frac{\partial \mathbf{v}}{\partial t} = -\nabla H - \frac{1}{Re}\nabla \times \boldsymbol{\omega} + \mathbf{v} \times \boldsymbol{\omega}, \tag{1}$$

$$\nabla \cdot \mathbf{v} = 0, \tag{2}$$

where equation (1) is based on the orthogonal decomposition of the vector field and equation (2) corresponds to mass conservation for incompressible fluids. Here $\mathbf{v}$ is the velocity and $\boldsymbol{\omega}$ is the vorticity, with $\boldsymbol{\omega} = \nabla \times \mathbf{v}$. H is the Bernoulli function (total energy), which is a sum of kinetic, static pressure and potential energies:

$$H = p/\rho + |\mathbf{v}|^2/2 + \Omega \tag{3}$$

where p is the pressure, ρ is the density of the fluid and Ω is the potential of the external force. $Re = U_0 L/\nu$ is the Reynolds number, where U_0 is the driven velocity, L is the length of the square cavity and ν is the kinematic viscosity. Taking the divergence of the momentum equation (1) leads to the Poisson equation for the Bernoulli function:

$$\nabla^2 H = \nabla \cdot (\mathbf{v} \times \boldsymbol{\omega}). \tag{4}$$

This Poisson equation with respect to the total energy will be important when we obtain the

pressure field at time $(n+1)\Delta t$. In the present method equation (4) is used as a supplementary equation.

These equations are subject to the Dirichlet and/or Neumann boundary conditions. The normal projection of equation (1) leads to the Neumann condition $\partial H/\partial n$, and the Dirichlet condition of H, if needed, is given by extrapolation at boundaries.[8] The boundary conditions for equation (4) are discussed in Reference 10.

3. GSMAC FINITE ELEMENT METHOD

3.1. Discretization of time

Before considering the fully discrete case, we first consider semidiscrete versions in time. Adopting the implicit formulation for the total energy and the explicit formulation for the velocity leads to the following equation:

$$\frac{\mathbf{v}^{n+1}-\mathbf{v}^n}{\Delta t} = -\nabla H^{n+1} - \frac{1}{Re}\nabla \times \boldsymbol{\omega}^n + \mathbf{v}^n \times \boldsymbol{\omega}^n. \tag{5}$$

Often the non-linear terms in the Navier–Stokes equations are treated explicitly using the third-order Adams–Bashforth method and the viscous term implicitly using the second-order Crank–Nicolson method. In the present method the vorticity is introduced as an explicit variable to simplify the algorithm. Equation (5) can be solved using the implicit pressure solution algorithm[11] and the explicit fractional time step method. As a result we obtain the following method.

A predictor of velocity is calculated from the forward Euler form:

$$\frac{\tilde{\mathbf{v}}-\mathbf{v}^n}{\Delta t} = -\nabla H^n - \frac{1}{Re}\nabla \times \boldsymbol{\omega}^n + \mathbf{v}^n \times \boldsymbol{\omega}^n. \tag{6}$$

Here $\tilde{\mathbf{v}}$ is a predictor of velocity at time $(n+1)\Delta t$. Correctors of the velocity and the Bernoulli function are calculated from a scalar potential ϕ:

$$\mathbf{v}^{n+1} = \tilde{\mathbf{v}} - \nabla\phi, \tag{7}$$

$$H^{n+1} = H^n + H^*, \tag{8}$$

where $H^* = \phi/\Delta t$. Since H is the total energy per unit volume, the change of H in dynamical processes is expected to be small compared with the change in pressure alone. Therefore the absolute value of H^* is also expected to be small, especially in regions of low energy dissipation.

The velocity field is solenoidal, so equation (7) is rewritten in the following form when we take the divergence of equation (7):

$$\nabla \cdot \mathbf{v}^{n+1} = 0, \tag{9}$$

which gives

$$\nabla^2 \phi = \nabla \cdot \tilde{\mathbf{v}}. \tag{10}$$

This Poisson equation (10) is solved by iteration using the modified cycle-to-cycle self-adjustment method[12] together with equations (7) and (8). The boundary condition of equation (10) is $\partial\phi/\partial n = 0$ on the rigid boundaries because of zero mass flux and $\phi = 0$ on the open boundaries because simultaneous relaxation of the velocity (7) and the Bernoulli function (8) means that $\tilde{\mathbf{v}} \to \mathbf{v}^{n+1}$ and $\tilde{H} \to H^{n+1}$, i.e. $\phi \to 0$ after some iterations (see step 4).

3.2. GSMAC algorithm

The iteration techniques employed in the present paper for rapid convergence and for stable time marching consist of the following steps.

Step 1: *Initial.* Assume all the values of velocity and pressure at time $n\Delta t$. Hence we can calculate the Bernoulli function and vorticity at time step n.

Step 2: *Predictor.* Solve equation (6) to obtain the first predictor of velocity from the values of H and $\mathbf{v}$ at time n.

Step 3: *Poisson equation.* Solve the Poisson equation (10) roughly by iteration using equation (23). This is the first iteration.

Step 4: *Corrector.* Correct the Bernoulli function and the velocity using equations (7) and (8). Check to see if the velocity field is solenoidal. If it is not solenoidal, return to step 3. This is the second iteration.

Step 5: *Momentum iteration.* If the convergence of $\| \nabla \cdot \mathbf{v} \| \ll \varepsilon$, where e.g. $\varepsilon = 10^{-4}$, is not enough after a few cycles of steps 3 and 4, first of all solve equation (4) by iteration giving an error criterion such as equation (38) with the predictor $\nabla \cdot (\tilde{\mathbf{v}} \times \boldsymbol{\omega})$ in order to find the predictor of H close to time $(n+1)\Delta t$. Then solve equation (6) using the updated values of H and $\mathbf{v}$ on the RHS of (6) to give a new predictor of velocity. Then repeat the same procedure from step 3. This is the third iteration, which indicates the full implicit formulation of the Navier–Stokes equations. The fifth step may usually be omitted for flows at low Reynolds numbers.

3.3. Discretization of space

The GSMAC discretization is a special case of the general weighted residual formulation and can be written as

$$\left(\psi, \frac{\partial v_i}{\partial t}\right)_w = -(\psi, \nabla_i H)_w + (\psi, \varepsilon_{ijk} v_j \omega_k)_w - \frac{1}{Re}(\psi, \varepsilon_{ijk}\omega_{k,j})_w. \tag{11}$$

Here ψ is a test function, ε_{ijk} is a permutation tensor and $(.,.)_w$ denotes the inner product with respect to the weight function w, that is

$$(\psi, v_i) = \int_{V_e} \psi v_i w \mathrm{d}V, \tag{12}$$

where V_e is the volume of element. The spatial discretization (12) is completely described by the choice of bases for ψ and v_i and the choice of the inner product weighting w. The choice of the same polynomials for ψ and v_i with $w = 1$ results in an isoparametric Galerkin method. For piecewise smooth finite approximations, the weak form is much more appropriate to reduce the degree of required continuity:

$$-(\psi, \nabla_i H) = (\nabla_i \psi, H) - \int_{S_e} \psi H n_i \mathrm{d}S, \tag{13}$$

$$(\psi, \varepsilon_{ijk}\omega_{k,j}) = -(\varepsilon_{ijk}\psi_{,j}, \omega_k) + \int_{S_e} \varepsilon_{ijk} n_i \psi \omega_k \mathrm{d}S, \tag{14}$$

where S_e is the boundary surface of element V_e. The interpolation function for ψ and v_i in the GSMAC method is bilinear in 2D or trilinear in 3D; H and ω_i are taken constant over each element and defined at the centre of each element. Substituting equations (13) and (14) into equation (11) leads to the following matrix equation:

$$\overline{M_{\alpha\beta}}\frac{\tilde{\mathbf{v}}_\beta-\mathbf{v}_\beta^n}{\Delta t}=\nabla_\alpha H_e^n+\frac{1}{Re}(\nabla_\alpha\times\omega_e^n)+M_{\alpha\beta}(\mathbf{v}_\beta^n\times\omega_e^n)-\mathbf{S}_\alpha^n, \tag{15}$$

where $\overline{M_{\alpha\beta}}$ is the lumped mass matrix of $M_{\alpha\beta}$. This discretized equation corresponds to equation (6). In equation (15),

$$M_{\alpha\beta}=\int_{V_e}N_\alpha N_\beta \mathrm{d}V \qquad \text{(mass matrix)}, \tag{16}$$

$$\mathbf{v}_\beta=[u_\beta, v_\beta, w_\beta] \qquad \text{(velocity vector)}, \tag{17}$$

$$\nabla_\alpha=\int_{V_e}\nabla N_\alpha \mathrm{d}V \qquad \text{(del operator)}, \tag{18}$$

$$\omega_e=\frac{1}{V_e}\int_{S_e}\mathrm{d}S\mathbf{n}\times\mathbf{v} \qquad \text{(vorticity vector in 3D)}, \tag{19}$$

$$\omega_e=\frac{1}{S_e}\oint_{C_e}\mathbf{v}\cdot\mathbf{dr} \qquad \text{(vorticity in 2D)}, \tag{20}$$

$$\mathbf{S}_\alpha=\int_{S_2^e}N_\alpha\left(H\mathbf{n}+\frac{1}{Re}\mathbf{n}\times\omega\right)\mathrm{d}S \qquad \text{(boundary term)}, \tag{21}$$

$$\mathbf{n}=[l, m, n] \qquad \text{(unit normal vector of surface)}, \tag{22}$$

where C_e is the boundary line of element S_e in 2D and N_α and N_β are shape functions. Equation (15) is solved by the element-by-element method[13] to reduce computer memory requirements. The volume integration is carried out using one-point quadrature. The Gauss–Legendre integral formula is used for the surface integral terms. During the iteration steps, all matrices and some vectors appearing in equation (15) are kept constant. Therefore the calculation of coefficient matrices is done only once.

3.4. Poisson equation

The Poisson equation (10) is solved by the false-time method. The Gauss theorem leads to the following iteration formula:

$$\phi_e^{k+1}=\phi_e^k-\lambda\frac{\Delta\tau}{V_e}\left(\oint_{S_e}\tilde{\mathbf{v}}\cdot\mathbf{n}\mathrm{d}S-\oint_{S_e}\frac{\partial\phi_e^k}{\partial n}\mathrm{d}S\right), \tag{23}$$

where λ is a parameter of relaxation and $\Delta\tau$ is an increment of false time. From the stability condition of von Neumann, $\Delta\tau\lambda/\sqrt{S_e}\leqslant 0{\cdot}25$ in 2D and $\Delta\tau\lambda/3\sqrt{V_e}\leqslant 0{\cdot}33$ in 3D for a homogeneous mesh. After some iterations according to the criterion of equation (38), we obtain a rough solution of ϕ_e:

$$\phi_e^{k+1}\approx\phi_e^k\approx\phi_e. \tag{24}$$

Then, using equation (7) and (8), we get new predictors of velocity and Bernoulli function. The most important part of the GSMAC method is the calculation of $\partial\phi/\partial n$ on the surface in

equation (23). The definition of gradient is given by

$$\text{grad}\,\phi = \lim_{V\to 0}\frac{1}{V}\oint\!\!\int \phi \mathbf{n}\,dS, \tag{25}$$

and this definition leads to the formula[14]

$$\int_{S_{abcd}}\frac{\partial\phi}{\partial n}dS = A_1(\phi_L-\phi_K)+A_2(\phi_a-\phi_c)+A_3(\phi_b-\phi_d) \tag{26}$$

for the surface integral of element V^K in Figure 2(a). Here the coefficients are

$$A_1 = \frac{1}{12V_{octa}}(\vec{ac}\times\vec{bd})\cdot(\vec{ac}\times\vec{bd}), \tag{27}$$

$$A_2 = \frac{1}{12V_{octa}}(\vec{ac}\times\vec{bd})\cdot(\vec{bd}\times\vec{LK}), \tag{28}$$

$$A_3 = \frac{1}{12V_{octa}}(\vec{ac}\times\vec{bd})\cdot(\vec{ac}\times\vec{KL}). \tag{29}$$

The volume of octahedron KabcdL is

$$V_{octa} = \tfrac{1}{6}\vec{KL}\cdot(\vec{ac}\times\vec{bd}). \tag{30}$$

When the vector $\vec{KL}$ is normal to the surface $\vec{ac}\times\vec{bd}$, the coefficients A_2 and A_3 become zero. For the two-dimensional case in Figure 2(b) we have

$$\int_{ab}\frac{\partial\phi}{\partial n}d\Gamma = A_1(\phi_L-\phi_K)+A_2(\phi_b-\phi_a), \tag{31}$$

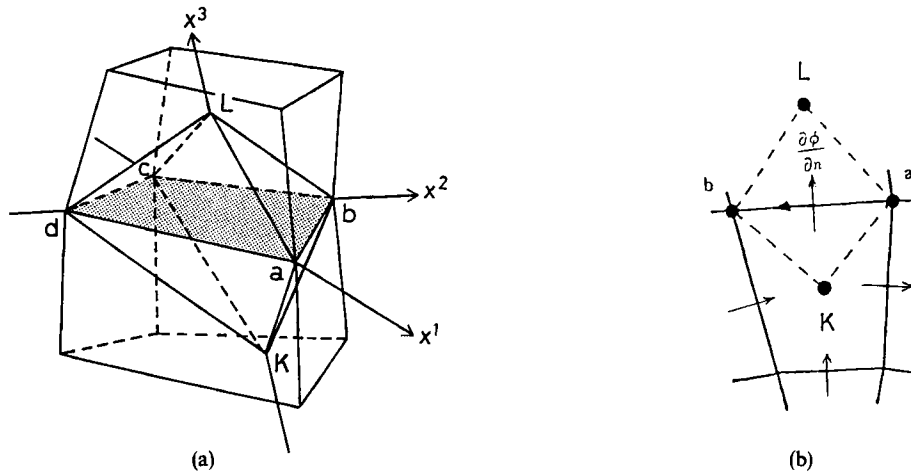

Figure 2. Flux calculation in 3D and 2D: (a) Flux calculation in 3D; (b) Flux calculation in 2D

where the coefficients are

$$A_1=\frac{\vec{ba}\cdot\vec{ba}}{2S_{KaLb}}, \tag{32}$$

$$A_2=\frac{\vec{KL}\cdot\vec{ba}}{2S_{KaLb}}. \tag{33}$$

The area of quadrilateral KaLb is

$$S_{KaLb}=\tfrac{1}{2}|\vec{KL}\times\vec{ba}|. \tag{34}$$

When the vector $\vec{ab}$ is orthogonal to the vector $\vec{KL}$, the coefficient A_2 is equal to zero.

3.5. *Interpolation of* ϕ

The values of ϕ^e are defined at the centre of each element, but we need the values of ϕ_i at each node when we execute a calculation of the Poisson equation (23). See Figure 3 for the two-dimensional case. The principle of the least squares of error,

$$\text{Minimum}\int_V(N_i\phi_i-N^e\phi^e)^2\,\mathrm{d}V, \tag{35}$$

leads to the matrix equation

$$M_{ij}\phi_j=B_i, \tag{36}$$

where M_{ij} is a mass matrix and

$$B_i=\int_{V_e}N_iN^e\phi^e\,\mathrm{d}V. \tag{37}$$

Equation (36) is solved by the three-pass algorithm.[15]

3.6. *Criterion of convergence and stability condition*

A criterion of convergence for the Poisson equation in the first iteration is

$$\frac{\Sigma_e|\oint_{S_e}\mathbf{n}\cdot\tilde{\mathbf{v}}\,\mathrm{d}S-\oint_{S_e}(\partial\phi/\partial n)\mathrm{d}S|}{\Sigma_eV_e}\leqslant\varepsilon_1. \tag{38}$$

The second criterion of convergence for the solenoidal velocity field in the second iteration is

$$\max|\mathrm{div}\,\mathbf{v}^{n+1}|_e\leqslant\varepsilon_2. \tag{39}$$

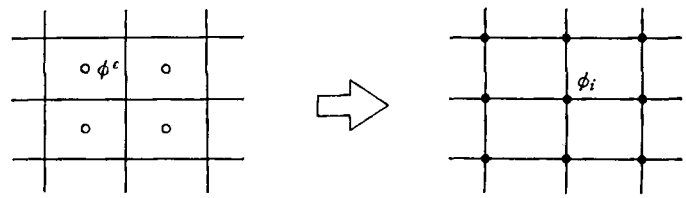

Figure 3. Interpolation of ϕ from element to node

Letting $h^e = V_e^{1/3}$ be a characteristic length of element, the conditions for time increment that we enforce are

$$\Delta t_c \leqslant \frac{h^e_{\min}}{|\mathbf{v}|_{\max}} \tag{40}$$

for the Courant number and

$$\Delta t_d \leqslant \tfrac{1}{8} Re (h^e_{\min})^2 \tag{41}$$

for the diffusion number. This gives the following inequality as a *stability* condition for the time increment:

$$\Delta t \leqslant \min(\Delta t_c, \Delta t_d). \tag{42}$$

4. RESULTS AND DISCUSSION

4.1. GSMAC element

As an example of the present method we consider here a driven cavity flow as shown in Figure 4(a). The GSMAC element used here is a quadrilateral element as shown in Figure 1(b). This element is easily extensible to three dimensions, in which case we would use the octahedral element shown in Figure 2(a). The lowest interpolation functions are adopted in this element, i.e. piecewise bilinear for the velocity and constant over each element for the total energy. The essential points behind the GSMAC method are that when the Poisson equation is solved, the values of scalar potential ϕ^e in the elements are transformed to values of ϕ_i at the nodes as shown in Figure 3 using the least-squares method, and the volume integral is transformed into the surface integral as shown in Figure 2(b) using the Gauss theorem in order to calculate mass flux on the surface.

4.2. Dependence of solutions on mesh

The accuracy of solutions depends on the design of mesh. Four types of mesh are used for calculation as shown in Figure 5. Types A and B are coarse and types C and D are fine. Types A

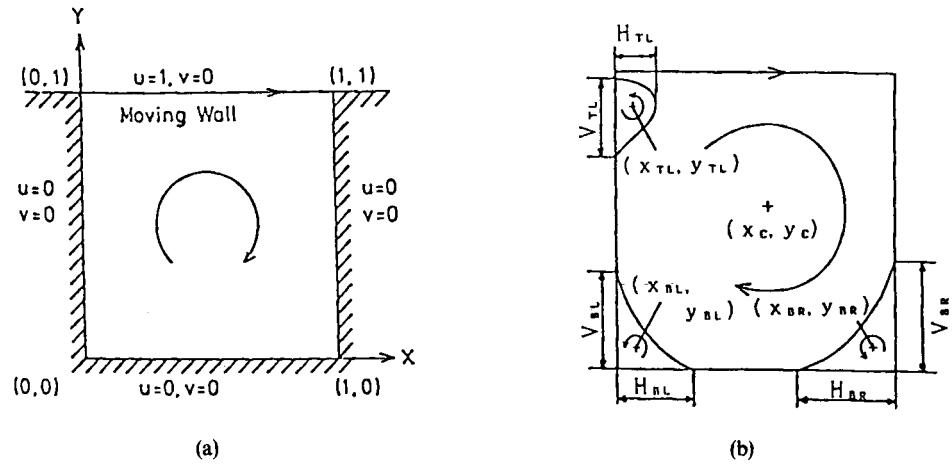

Figure 4. Driven cavity flow model: (a) Boundary conditions; (b) Flow configuration and nomenclature

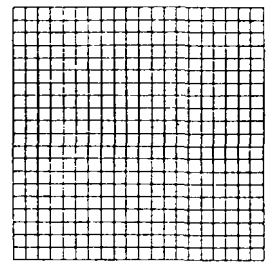

type A
(20×20, 400 element)

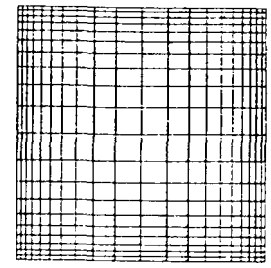

type B
(20 ×20, 400 element)

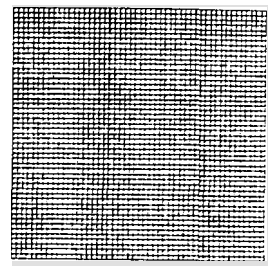

type C
(50×50, 2500 element)

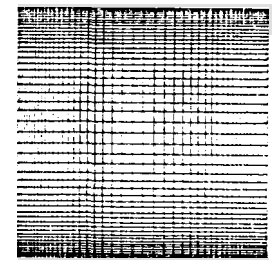

type D
(50×50, 2500 element)

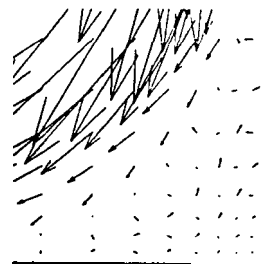

type B

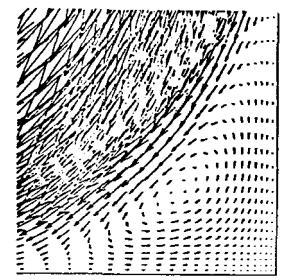

type D

Figure 5. Dependence of solutions on mesh; $Re = 1000$

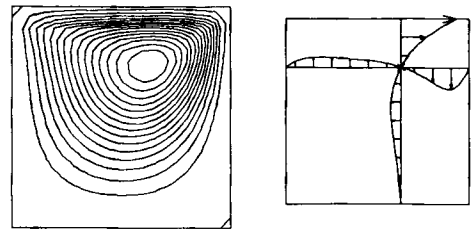

(a) $R_e=100$, $t=5$

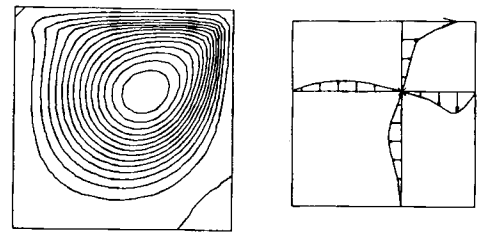

(b) $R_e=400$, $t=20$

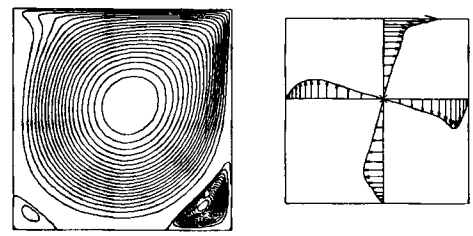

(c) $R_e=1\,000$, $t=40$

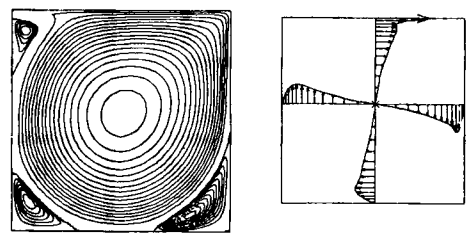

(d) $R_e=5\,000$, $t=80$

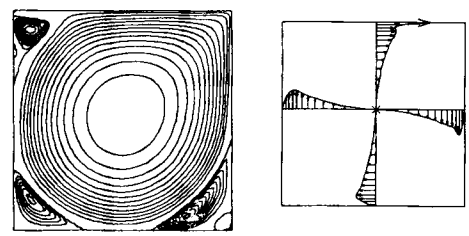

(e) $R_e=10\,000$, $t=120$

(a) (b)

Figure 6. Steady state solutions: (a) Stream line; (b) velocity distribution

and C are bilinear meshes with equi-intervals and types B and D are log–log meshes with different intervals which become fine near the boundary. We obtained good results using coarse meshes at Reynolds numbers from 100 to 500, but, as shown in Figure 5, velocity wiggles appear at a Reynolds number of 1000. Hence we use type D for Reynolds numbers higher than 1000.

4.3. Flow dependence on Reynolds number

Figure 6 shows how flows in the cavity depend on the Reynolds number. The flow configuration is characterized by the locations of the centres of the main vortex and the secondary vortices, and by their sizes. Comparison of the characteristic values with results Ghia *et al.*[16] is shown in Table I according to the nomenclature in Figure 4(b). Here we should note the following fact: Ghia *et al.* used 129×129 mesh at $Re = 1000$ and a 257×257 mesh at $Re \geqslant 5000$. Although we used only a 50×50 mesh, the accuracy of the solutions appears almost the same as theirs. Figure 7 shows

Table I. Comparison of characteristic values

Re	Parameter	GSMAC	Ghia *et al.*[16]
(a) 100	(x_C, y_C)	(0·6269, 0·7371)	(0·6172, 0·7344)
(b) 400	(x_C, y_C)	(0·5967, 0·6211)	(0·5547, 0·6055)
	(x_{BR}, y_{BR})	(0·8926, 0·1137)	(0·8906, 0·1250)
	H_{BR}	0·2540	0·2167
	V_{BR}	0·2528	0·3203
(c) 1000	(x_C, y_C)	(0·5335, 0·5653)	(0·5313, 0·5625)
	(x_{BR}, y_{BR})	(0·8672, 0·1119)	(0·8594, 0·1094)
	(x_{BL}, y_{BL})	(0·0822, 0·0731)	(0·0859, 0·0781)
	H_{BR}	0·3091	0·3034
	V_{BR}	0·3410	0·3536
	H_{BL}	0·2045	0·2188
	V_{BL}	0·1523	0·1680
(d) 5000	(x_C, y_C)	(0·5120, 0·5337)	(0·5117, 0·5352)
	(x_{BR}, y_{BR})	(0·8134, 0·753)	(0·8086, 0·0742)
	(x_{BL}, y_{BL})	(0·0750, 0·1378)	(0·0703, 0·1367)
	(x_{TL}, y_{TL})	(0·0658, 0·9045)	(0·0625, 0·9102)
	H_{BR}	0·3496	0·3565
	V_{BR}	0·4350	0·4180
	H_{BL}	0·3159	0·3184
	V_{BL}	0·2693	0·2643
	H_{TL}	0·1208	0·1211
	V_{TL}	0·2555	0·2693
(e) 10000	(x_C, y_C)	(0·5125, 0·5274)	(0·5117, 0·5333)
	(x_{BR}, y_{BR})	(0·7944, 0·0640)	(0·7656, 0·0586)
	(x_{BL}, y_{BL})	(0·0790, 0·1400)	(0·0586, 0·1641)
	(x_{TL}, y_{TL})	(0·0758, 0·9120)	(0·0703, 0·9141)
	H_{BR}	0·3773	0·3906
	V_{BR}	0·4529	0·4492
	H_{BL}	0·3515	0·3438
	V_{BL}	0·2834	0·2891
	H_{TL}	0·1683	0·1589
	V_{TL}	0·3463	0·3203

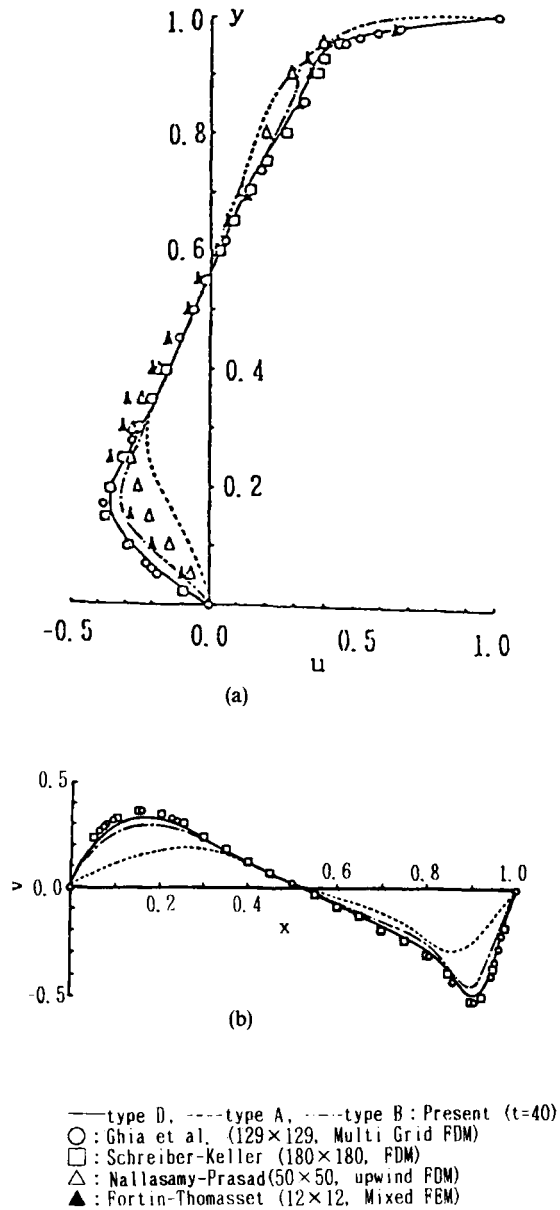

Figure 7. Distributions of x- and y-components of velocity: (a) x-component of velocity; (b) y-component of velocity

the distributions of x- and y-components of velocity on the centrelines of the cavity. These also shows good agreement with the results of type D.

The results of Nallasamy and Prasad[17] and Fortin and Thommasset[18] are excellent but differ slightly from the results of Ghia *et al.*[16] and Schreiber and Keller[19] in the x-component of velocity. Steady solutions at $Re=1000$, 5000 and 10000 are shown in detail in Figure 8. Values of streamlines and vorticity lines are given in Table II. In Figure 9(a) comparison of the height of the

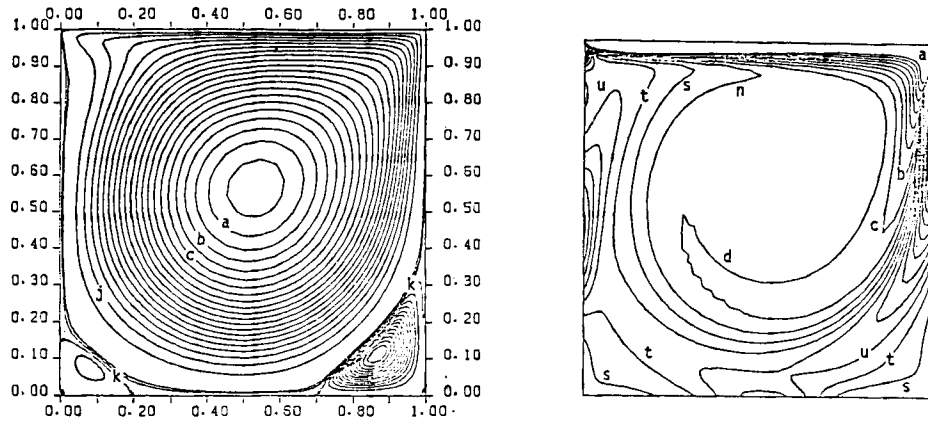

$R_e=1000,\ t=40$

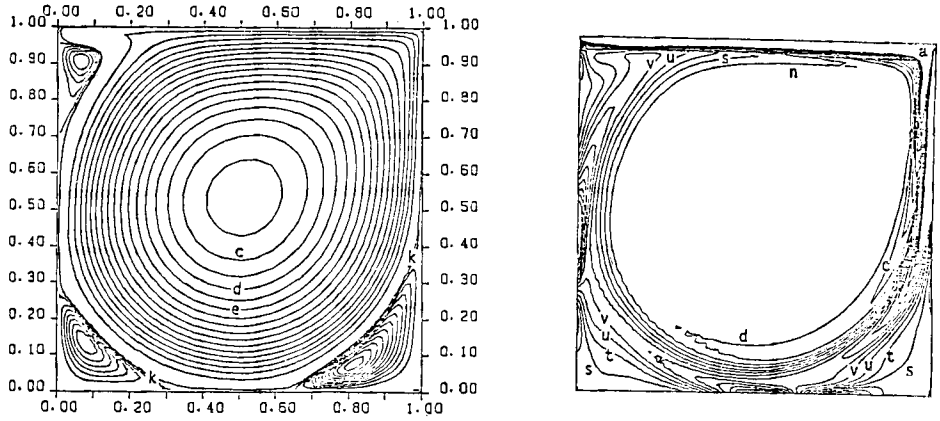

$R_e=5000,\ t=80$

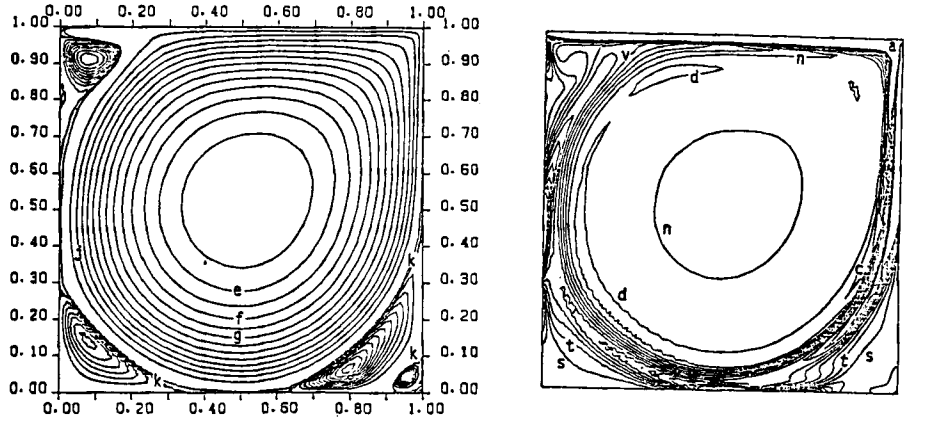

$R_e=10000,\ t=120$

(a) (b)

Figure 8. Steady solutions at $Re=1000$, 5000 and 10 000 (a) stream line; (b) Vorticity line

Table II. Streamfunction and vorticity

	Stream function	Vorticity		Streamfunction	Vorticity
a	−0·1	−10·0	l	$0{\cdot}2\times10^{-3}$	−1·2
b	−0·09	−4·0	m	$0{\cdot}4\times10^{-3}$	−1·1
c	−0·08	−3·0	n	$0{\cdot}6\times10^{-3}$	−1·0
d	−0·07	−2·0	o	$0{\cdot}8\times10^{-3}$	−0·8
e	−0·06	−1·9	p	$1{\cdot}0\times10^{-3}$	−0·6
f	−0·05	−1·8	q	$1{\cdot}2\times10^{-3}$	−0·4
g	−0·04	−1·7	r	$1{\cdot}4\times10^{-3}$	−0·2
h	−0·03	−1·6	s	$1{\cdot}6\times10^{-3}$	0·0
i	−0·02	−1·5	t	$1{\cdot}8\times10^{-3}$	1·0
j	−0·01	−1·4	u	$2{\cdot}0\times10^{-3}$	2·0
k	0·0	−1·3	v	$2{\cdot}2\times10^{-3}$	3·0

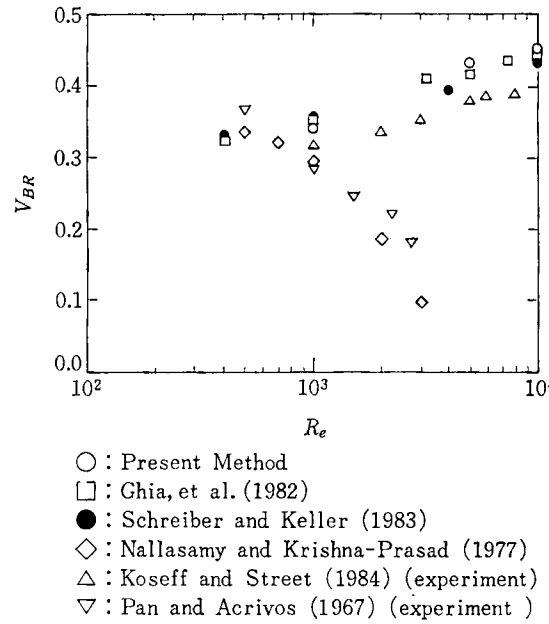

Figure 9. Height of the secondary vortex at the lower right corner

secondary vortex at the lower right corner with experimental results of Koseff and Street[20] and Pan and Acrivos[21] is shown. There is a bifurcation point near $Re = 1000$. Both experimental and old theoretical data by Nallasamy and Prasad[17] and Pan and Acrivos[21] show a decrease, whereas recent data by Ghia *et al.*[16], Schreiber and Keller[19] and Koseff and Street[20] and our results show an increase, as the Reynolds number increases.

4.4. Transient phenomena

In this case the fluid in the cavity is at rest initially and the surface at the top of the cavity is suddenly set in motion. Hence fluid in the cavity begins moving by shear stress owing to the

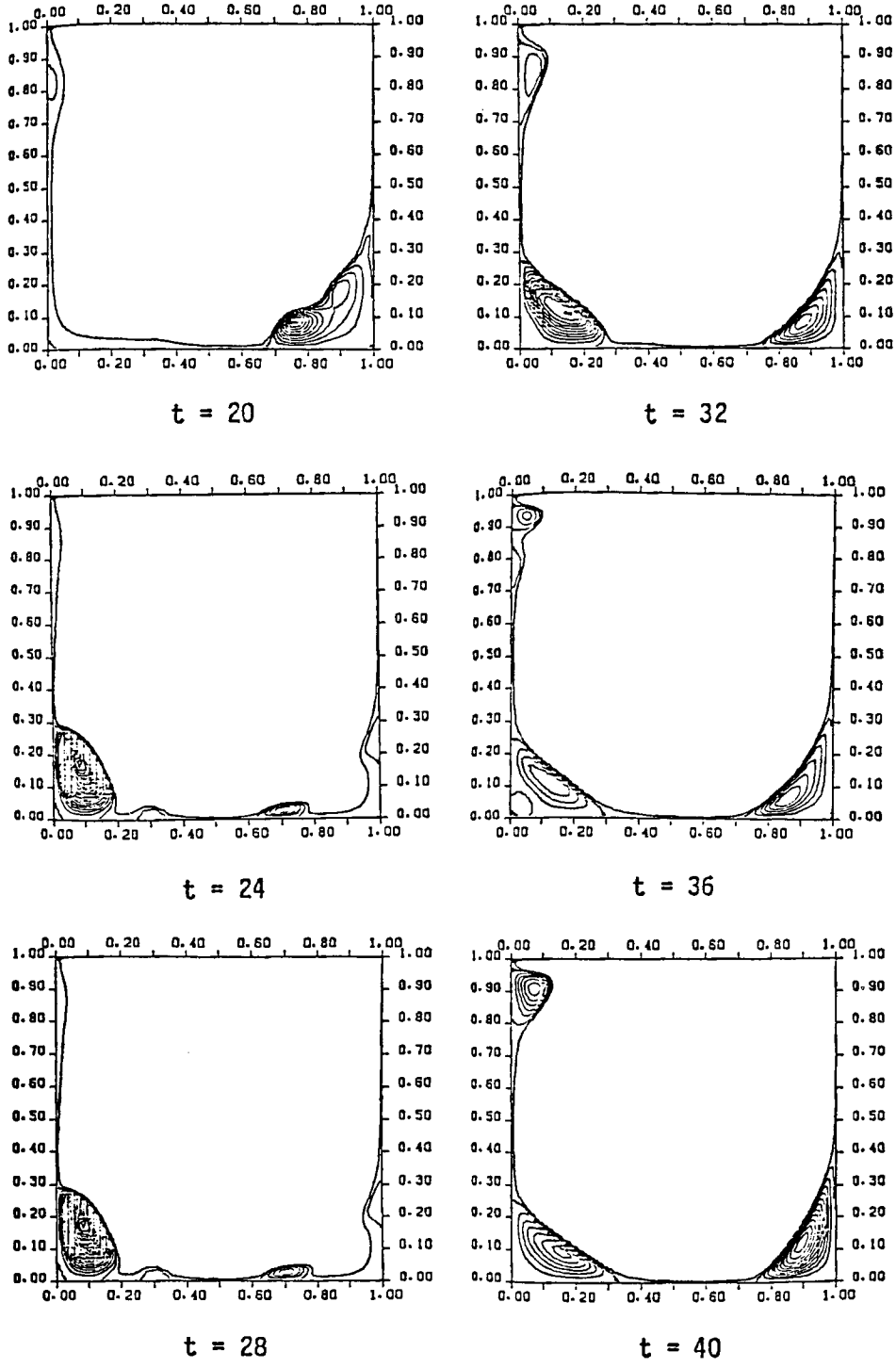

Figure 10. Time evolution of corner vortices; $Re = 10\,000$, $\Delta\psi = 0{\cdot}0002$

viscosity of the fluid. The motion of the fluid reaches a steady state gradually. The time marching in the GSMAC method is used for unsteady flows, so we can investigate the transient phenomena of driven cavity flows. Three secondary vortices appear in the cavity. These vortices are not stable in the transient state. Their evolution with time is shown in Figure 10. By the time $t=40$ we can observe that their shapes have developed towards the final values. Loci of the main vortex at

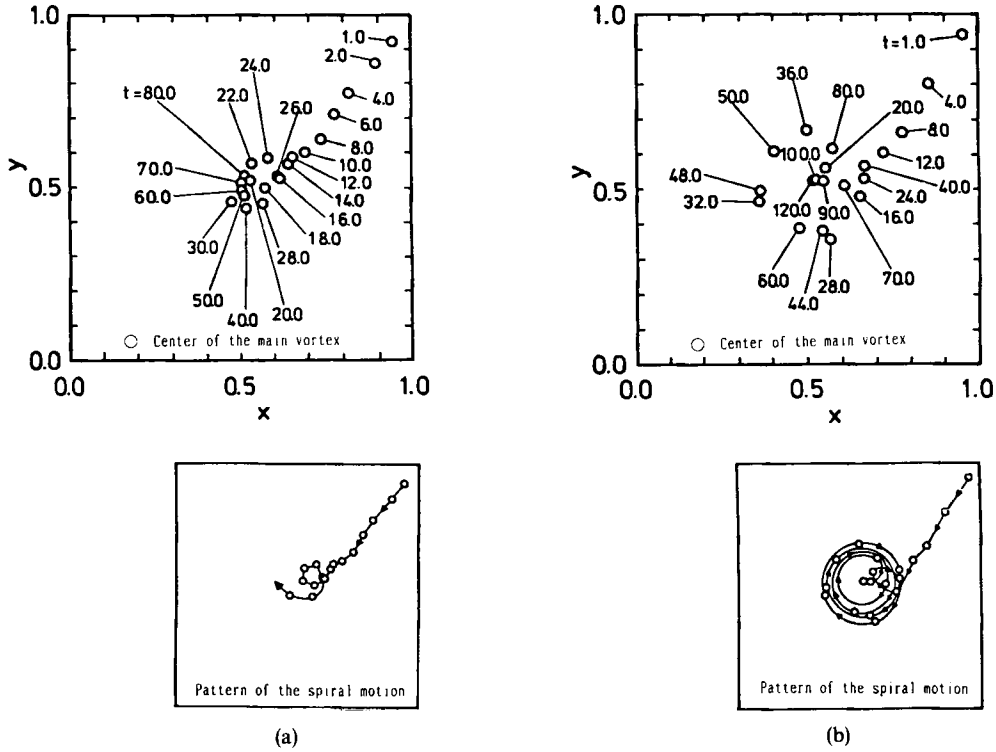

Figure 11. Loci of the centre of the main vortex: (a) Re = 5000; (b) Re = 10 000

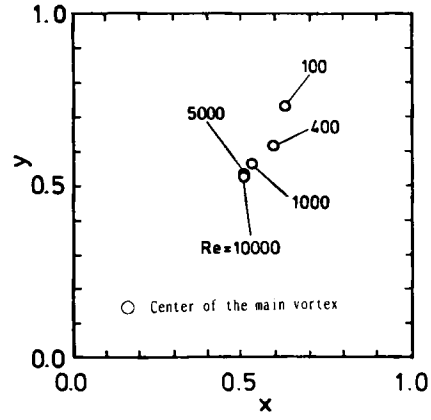

Figure 12. Location of the centre of the main vortex

$Re = 5000$ and 10000 are shown in Figure 11. They are spiral. The motion at $Re = 5000$ becomes steady after one cycle. In comparison, the motion at $Re = 10000$ reaches a steady state gradually after some rotations. The location of the centre of the main vortex is shown in Figure 12 for each Reynolds number. The centre of the main vortex at $Re = 10000$ is almost at the centre of the square cavity at the time $t = 120$.

4.5. Flow past a circular cylinder

As an example of distorted general meshes, we present next a start-up flow around a circular cylinder which is caused by the pressure gradient. The model and the boundary conditions are shown in Figure 13 and the mesh used is shown in Figure 14. The boundary term of equation (21) is rewritten for the traction-free outflow condition as follows:

$$\mathbf{S}_\alpha = \int_{S_2^e} N_\alpha H \mathbf{n} \mathrm{d}S + \frac{1}{Re} \int_{S_2^e} N_\alpha \mathbf{n} \times \boldsymbol{\omega} \mathrm{d}S. \tag{43}$$

When the traction on the surface is zero, the second term on the RHS of equation (43) becomes zero and the value of H on the surface is simply given by extrapolation, which is very convenient. Initially the fluid in the region is at rest everywhere. The Reynolds number is chosen as 3000

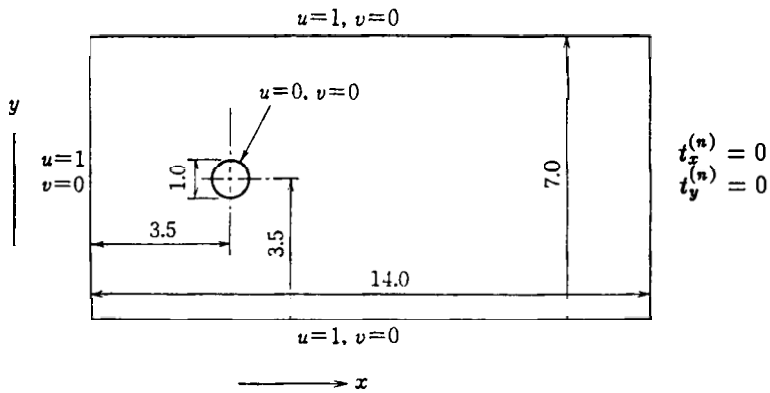

Figure 13. Flow past a circular cylinder: analytical model and boundary conditions

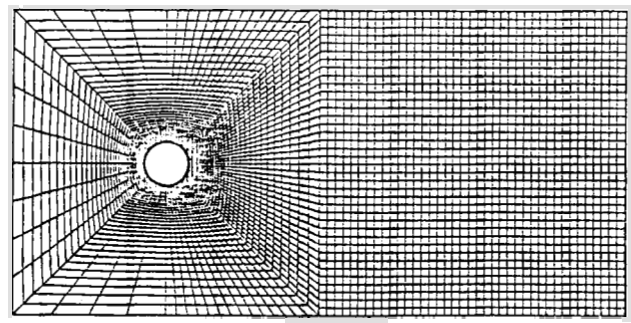

Figure 14. Finite element mesh; 4680 elements and 4801 node points

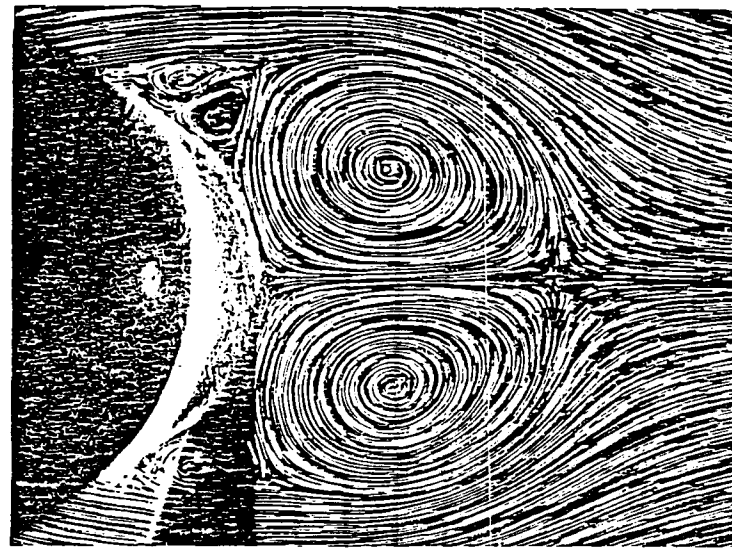

Figure 15. Experimental photograph of Bouard and Coutanceau;[22] $t=2{\cdot}5$, $Re=3000$

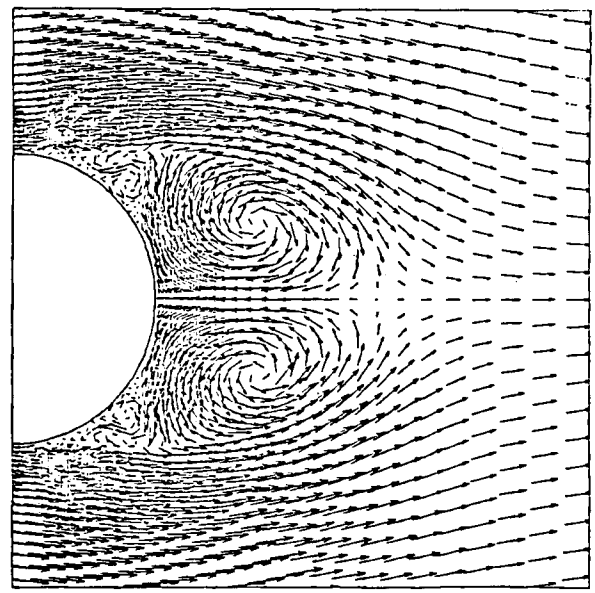

Figure 16. Present method (velocity vectors); $t=2{\cdot}5$, $Re=3000$

in order to allow comparison with the visualized flow done by Bouard and Coutanceau[22] (see Figure 15). One pattern of velocity vectors is shown as a numerical result in Figure 16. The twin vortices and the secondary vortices near the separation points are very similar to the experimental ones. Figure 17 is a comparison of streamlines through the separation point. The geometrical configuration and the time evolution of a twin vortex are shown in Figures 18 and 19 respectively.

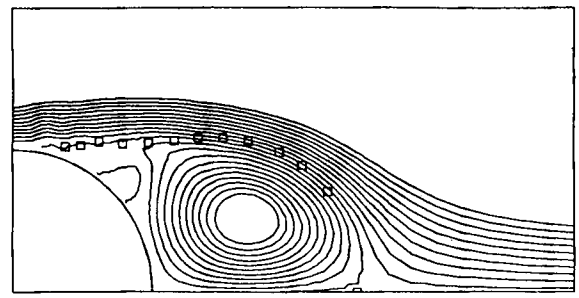

Figure 17. Comparison of streamlines though the separation point; $t = 2{\cdot}5$, $Re = 3000$, $\Delta\psi = 0{\cdot}02$. The open squares are the experimental results of Bouard and Coutanceau[22]

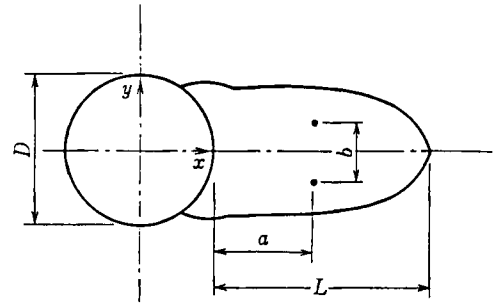

L : Length of Closed Wake
a : Location of Vortex Center Measured from the Rear of Cylinder
b : Distance between Vortex Centers
D : Diameter of Cylider

Figure 18. Geometrical configuration of a twin vortex

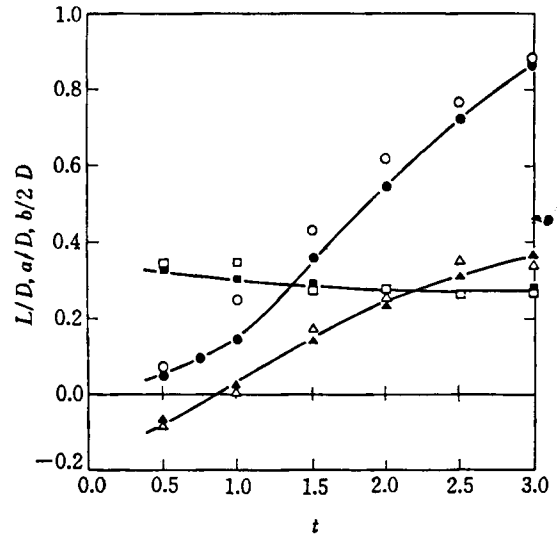

Present Method : ○, L/D; △, a/D; □, $b/2\,D$
Experiments of Bouard and Coutanceau(1980) :
●, L/D; ▲, a/D; ■, $b/2\,D$

Figure 19. Time evolution of a twin vortex; $Re = 3000$

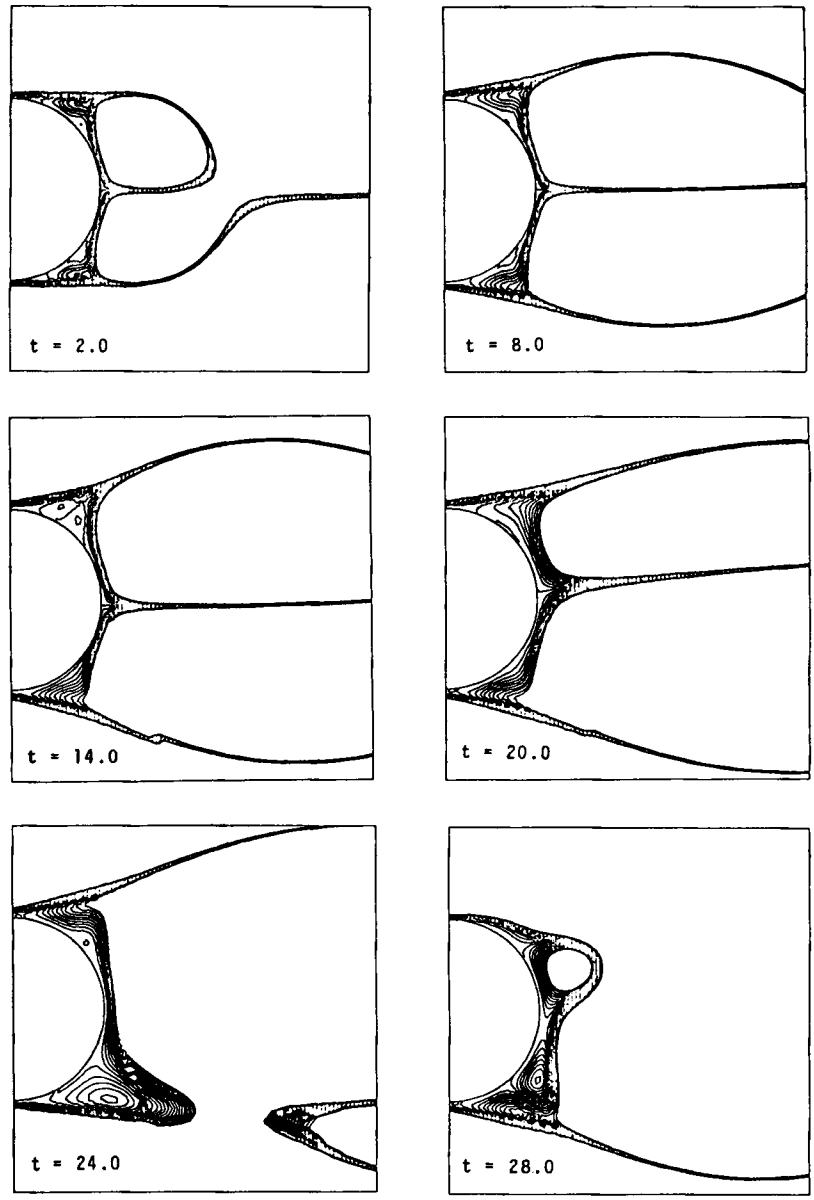

Figure 20. Example of vortex shedding behind a circular cylinder; $Re = 550$, $\Delta\psi = 0{\cdot}001$

Although the narrow width of the calculated region makes the length of wake long, on the whole we have good agreement with experiment.

To conclude, Figure 20 shows an example of vortex shedding behind a circular cylinder at $Re = 550$ where a longer time was simulated.

5. CONCLUSIONS

The GSMAC finite element method presented here is confirmed to be suitable as an incompressible Navier–Stokes solver at high Reynolds numbers. This new method is composed of:

(a) orthogonal decomposition of the flow field described by the rotational form of the momentum equation
(b) implicit formulation for the Bernoulli function and explicit formulation for the velocity and vorticity
(c) modified cycle-to-cycle self-adjustment using a false-time method
(d) implicit pressure solution algorithm by iteration
(e) explicit fractional time step method expressed by predictor and corrector of the velocity
(f) a generalization of the MAC method to a finite element method
(g) mass-lumping technique and multipass algorithm
(h) one-point quadrature
(i) an element-by-element solution method to reduce memory requirements.

We will show some examples of three-dimensional flow in a future paper, including effects of heat convection and electromagnetic interaction with fluid.

ACKNOWLEDGEMENTS

It is a pleasure to acknowledge helpful discussions and correspondence with Dr. Philip M. Gresho of Lawrence Livermore National Laboratory.

This work has been partly supported by the Iwatani Naoji Foundation's Research Grant and by Grant-in-Aid for Scientific Research from the Ministry of Education, Science and Culture of Japan.

REFERENCES

1. T. Tanahashi and T. Saito, *Rep. Inst. Numer. Anal. Kyoto Univ.*, **548**, 122 (1985).
2. R. Piva *et al.*, *Comput. Fluids*, **8**, 225 (1980).
3. A. E. Amsden and F. H. Harlow, *Report LA-4370*, Los Alamos Scientific Laboratory, 1970.
4. F. H. Harlow and J. E. Welch, *Phys. Fluids*, **8**, 2182 (1965).
5. C. W. Hirt, B. O. Nichols and N. C. Romero, *Report LA-5852*, Los Alamos Scientific Laboratory, 1975.
6. E. Kanai and T. Tanahashi, *Trans. JSME B*, **53**, 683 (1987).
7. T. Tanahashi, M. M. Dede and R. Holmes, *Report No. ME*/87/2, Department of Mechanical Engineering, University of Southampton,1987.
8. M. J. P. Cullen, *J. Comput. Phys.*, **51**, 291 (1983).
9. P. A. Raviart, *Springer Lecture Notes in Physics*, **91**, 27 (1977).
10. A. J. Choin and J. E. Marsden, *A Mathematical Introduction to Fluid Mechanics*, Springer, New York, 1979.
11. R. I. Issa, *J. Comput. Phys.*, **62**, 40 (1985).
12. T. Tanahashi, *Kikai no Kenkyu*, **37**, 383, 501 (1985).
13. T. J. R. Hughes *et al.*, *J. Eng. Mech.*, **109**, 576 (1983).
14. T. Tanahashi, *Continum Mechanics* (5), Rikotosho, 1988, p. 246.
15. J. Donea *et al.*, *Comput. Methods Appl. Mech. Eng.*, **45**, 123 (1984).
16. U. Ghia *et al.*, *J. Comput. Phys.*, **48**, 387 (1982).
17. M. Nallasamy and K. K. Prasad, *J. Fluid Mech.*, **79**, 391 (1977).
18. M. Fortin and F. Thommasset, *J. Comput. Phys.*, **31**, 113 (1979).
19. R. Schreiber and H. B. Keller, *J. Comput. Phys.*, **49**, 310 (1983).
20. J. R. Koseff and R. L. Street, *Trans. ASME, J. Fluid Eng.*, **106**, 21 (1984).
21. F. Pan and A. Acrivos, *J. Fluid Mech.*, **28**, 643 (1967).
22. R. Bouard and M. Coutanceau, *J. Fluid Mech.*, **101**, 583 (1980).